

**Electrochemical Mitigation of Hydrogen Environment
Embrittlement of Ultra-high Strength AerMetTM 100**

Sami Al-Ghamdi and John R. Scully

DISTRIBUTION STATEMENT A
Approved for Public Release
Distribution Unlimited

20060713053

**EFFECT OF SELECTED INHIBITORS ON HYDROGEN PRODUCTION,
ABSORPTION AND ENVIRONMENTAL EMBRITTLEMENT OF
AN ULTRA HIGH STRENGTH STEEL**

Sami Al-Ghamdi and John R. Scully

DISTRIBUTION STATEMENT A
Approved for Public Release
Distribution Unlimited

ABSTRACT

The goal of this research is to extend the potential region of high toughness in an ultra-high strength steel (UHSS) to anodic and cathodic potentials where hydrogen environment embrittlement (HEE) is normally observed due to hydrogen uptake in the absence of inhibitors. This is being explored through the investigation of several selected chemical inhibitors (anodic inhibitors and cathodic blocking agents). The research is conducted in three stages. The effect of inhibition on lowering hydrogen production and ingress (absorption) is determined using planar coupons under conditions representative of crack tips. Studies are then extended to rescaled crevices that model occluded sites of much smaller dimensions (will not be discussed in this paper). Finally, verification of chemical inhibition of HEE susceptibility, in fracture experiments, is exhibited by a restoration in toughness and/or a reduction in crack growth rate on fatigue pre-cracked specimen. Fracture experiments are performed at various applied potentials in a marine environment. This research is part of an overall scheme to combine the study of inhibition with the control of metallurgical purity and hydrogen trap states, as well as tailored cathodic protection to optimize the fracture toughness of UHSS in marine environments. The long term goal is to provide a coupled strategy to mitigate HEE of modern high strength steels.

BACKGROUND

Ultra-high strength material

UNS K92580 is a secondary hardened martensitic steel. The alloy is initially austenitized @ 885°C, air-cooled for 2 hours, further quenched to -73°C, and then peak aged @ 482°C to

achieve optimal strength and fracture toughness as shown in Table 1. The chemical composition and mechanical properties for the peak aged condition are given in Tables 2 and 3.

The alloy was developed to provide high fracture toughness, $K_{IC} \approx 130 \text{ MPa}\sqrt{\text{m}}$, compared to older generation UHSS steels. This was achieved by advanced melting in vacuum to minimize contaminant inclusions, mainly sulfur and phosphorous compounds [6,15]. The high fracture toughness is mainly attributed to the presence of fine (3 nm) reverted austenite uniformly dispersed coherent particles. The austenite was shown to be rich in C, Ni, and Co. These elements reduce martensite deformation temperature (M_d) and lead to the increase in austenite stability when straining specimen in fracture experiments. On the other hand, high strength, $\sigma_{YS} \approx 1765$, was due to the presence of the fine-cohesive M_2C carbides, which are the source of the secondary strengthening. Also, high strength was achieved due to the presence of extensive dislocation structures stabilized by the high concentration of Co in UNS K92580, around 13%wt. The microstructure is rich in hydrogen traps; prior-austenite grain boundaries, martensite laths, high dislocation density, coherent M_2C carbides and solute zones, and the thin film of precipitated reverted austenite on lath/plate boundaries as shown in Fig. 1 [10]. Each trap state possess it own hydrogen binding energy [2].

Table 1 – Heat treatment of UNS K92580

Process	Temperature (°C)	Duration (hours)
Austenitize (vacuum)	885	1
Air Cool	-	2
Cold Stabilize	-73	1
Age (air)	482	5

Table 2 – Chemical composition of UNS K92580 (weight percent)

Fe	C	Co	Ni	Cr	Mo	Ti	Si	S	P	H (ppmw)
bal.	0.23	12.80	10.89	2.78	1.21	0.010	0.016	0.0008	0.001	0.35

Table 3 – Mechanical properties of UNS K92580

HRC	σ_{UTS} (MPa)	σ_{YS} (MPa)	E (GPa)	K_{IC} (MPa $\sqrt{\text{m}}$)
54	1985	1765	194	130

Hydrogen embrittlement is a prime factor hindering the performance of UHSS alloy in naval service. UNS K92580 suffers an order of magnitude degradation in fracture toughness due to HEE caused by an increase in diffusible hydrogen concentration ($C_{H,diff}$), especially above 2 ppmw as shown in Fig. 2. Such hydrogen concentrations may be achieved by a combination of electrochemical polarization and occluded crack geometry in seawater.

Potential dependency of K_{TH} and C_H

HEE susceptibility is minimized if pre-cracked UHSS specimens are held close to their open circuit potential (OCP) which is near -0.7 to -0.6 V_{SCE}. The $C_{H,diff}$ in the fracture process zone (FPZ), implied from these experiments assuming a fracture model developed by Gerberich and adapted is minimal approaching zero near the OCP [8]. Therefore, the HEE and subsequent hydrogen environment-assisted cracking (HEAC) susceptibility of UNS K92580 are strongly potential dependant at both cathodic as well as anodic potentials as shown in Fig. 3. Hydrogen production can be severe at anodic potentials due to ohmic voltage drop and acidification at the crack tip, brought about principally by the hydrolysis of chromium ions into solutions [16]. Also, the slow hydrogen diffusion rate favors local uptake and accumulation at the crack tip. While, in cathodic conditions, there is a large hydrogen overpotential at external surfaces (η) and bulk charging occur. Increasing the applied potential even more cathodic results in an increasingly negative crack tip overpotentials for the same applied potential (E_{app}) [1].

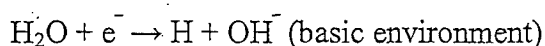
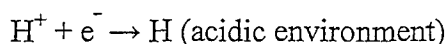
Hydrogen production and absorption at occluded sites

Electrochemical conditions lead to hydrogen production within the crack. This production rate is dependent upon local potential and pH. Production of H^+ and its absorption into metal under crack cathodic conditions is due to dissolution of sacrificial coating and cathodic polarization of the crack tip, as per the following reactions (Fig. 4a):

- *Anodic reaction (sacrificial coating):*



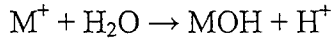
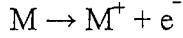
- *Cathodic reaction (crack tip and on bulk surfaces):*



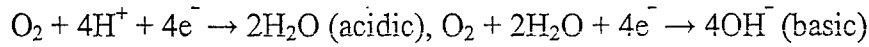
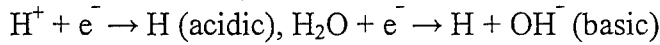
→ Cations migrate to crack tip

While, under crack anodic conditions, production of H^+ and absorption into the metal, at the crack tip, occurs with the presence of an oxide film or a noble coating (Fig. 4b).

- *Anodic reaction (crack tip):*



- *Cathodic reaction (bulk surfaces):*



→ Anions migrate to crack tip

Hydrogen concentration at the crack tip is enhanced by local stresses. The stress-enhanced hydrogen concentration ($C_{H,\sigma}$) depends on the lattice hydrogen concentration ($C_{H,lattice}$) and is enhanced by the hydrostatic stress (σ_H) at the crack tip, as follow [15]:

$$C_{H,lattice} = C_{H,diff} \left(\frac{D_H}{D_l} \right) \quad - \text{Eq. 1}$$

$$C_{H\sigma} = C_{H,lattice} \exp \left(\frac{\sigma_H V_H}{RT} \right) \quad - \text{Eq. 2}$$

where D_H is the hydrogen diffusivity, D_l is the lattice diffusivity, V_H is the partial molar volume of hydrogen, R is the gas constant, and T is the temperature.

Previous work has shown that the crack tip stress field can lead to a 35 to 2×10^5 – fold increase in hydrogen concentration over $C_{H,lattice}$ [5]. The dissolved hydrogen, as well as hydrogen trapped in weak trap sites with binding energies less than $\sigma_H V_H$, diffuses towards the crack tip stress field. Martensite lath interfaces are possible sites within the FPZ where hydrogen can segregate [4]. The total amount that segregates to these interfaces within the FPZ depends on the interaction between the crack tip stress field and the trap binding energy (E_b) of the lath interfaces, the concentration is further enhanced to $C_{H\sigma,T}$, as follow:

$$C_{H\sigma,T} = C_{H,lattice} \exp\left(\frac{E_b + \sigma_H V_H}{RT}\right) \quad - \text{Eq. 3}$$

The threshold stress intensity (K_{TH}) is then related to $C_{H\sigma,T}$ through the following [8]:

$$K_{TH} = \frac{1}{\beta'} \exp\left(\frac{(K_{IG} - \alpha C_{H\sigma,T})^2}{\alpha'' \sigma_{YS}}\right) \quad - \text{Eq. 4}$$

where K_{IG} is the critical Griffith stress-intensity factor for cleavage fracture without hydrogen, σ_{YS} is the yield strength, β' and α'' are constants related to analysis of dislocation structure about the crack tip, and α is a constant. Environmental hydrogen embrittlement thresholds (K_{TH}) are governed by the $C_{H,diff}$ at the crack tip FPZ.

Mitigation by Inhibition

Inhibitors function through different mechanisms to mitigate HEE of UHSS as seen in Table 4. Anodic inhibitors act to mitigate metal dissolution inhibiting hydrolysis that creates H^+ in an occluded site that could be reduced and absorbed into the UHSS. Cathodic inhibitors act to reduce the hydrogen uptake rate. This could be achieved by reducing the overall reaction rate (J_c), mitigating hydrogen absorption rate (k_{abs}), enhancing desorption rate (k_{des}) and/or recombination rate (k_r) leading to a reduction in the concentration of diffusible hydrogen in the UHSS. Inhibition could also be achieved by Cl^- absorption, pH buffering, and surface passivation [3,11,14].

A separate screening method was developed for selected anodic and cathodic inhibitors. The sought-after end result is test samples of UNS K92580 in simulated marine environment, with preferred inhibitor(s), in a fracture experiment to determine and characterize mitigation of HEE.

Table 4 – Inhibitor types with examples

Inhibitor function	Example compounds or species
Cathodic inhibitor	Polyphosphate, zinc, silicate
Anodic inhibitor	Chromate, nitrate, molybdate, cerate, orthophosphate, ferrocyanide
Chloride absorbers	Not determined
Acid Buffers	Borax, Sodium bicarbonate, etc.
Hydrogen entry inhibitors (not including passivators)	Bi, Pb, Zn, Noble metals, Various organic film formers
Recombination promoters	Ir, Pd, Pt

A combination of traditional and new types of inhibitors was chosen for evaluation as seen in Table 5. While chromate and molybdate are traditionally favored inhibitors, new rare earth metal (REM) organic inhibitors were also chosen to compare the performance of each set of experimental results [3,11,14,17].

Table 5 – List of selected chemical inhibitors [17]

No.	Inhibitor	Inhibitor Name	Proposed Action	Source
1	Ce(acetate) ₃	Cerium acetate	Cathodic reaction inhibitor, physical barrier	Various
2	Zn(acetate) ₃	Zinc acetate	Cathodic reaction inhibitor	Various
3	Ce(dbp) ₃	Cerium dibutyl phosphate	Cathodic reaction inhibitor, physical barrier	University of Monash
4	REM Organic	Rare Earth Metal Organic	Cathodic reaction inhibitor, physical barrier	University of Monash
5	Na ₂ MoO ₄	Sodium molybdate	Anodic inhibitor, passive film	Lynch, Parrish, Agarwala, others
6	Na ₂ CrO ₄	Sodium chromate	Anodic inhibitor, passive film	Lynch, Parrish, Agarwala, others
7	Mn Molyblue	Manganese Molybdenum Blue	Anodic inhibitor, passive film	Rockwell Scientific (Kendig)
8	Y Molyblue	Yttrium Molybdenum Blue	Anodic inhibitor, passive film	Rockwell Scientific (Kendig)

Therefore, one challenge is to develop chemical inhibitors that operate to reduce HEAC during polarization. The goal of this research is to extend the potential region of high fracture toughness to anodic and cathodic potentials where HEE is normally observed in the absence of inhibitors (Fig. 3).

EXPERIMENTAL METHODS

Electrochemical Polarization (Potentiodynamic) in Selected Inhibitors

Initially, a small sample of UNS K92580 was cut (2mm wide x 10mm long x 0.2mm thick), tack-welded to a nickel wire and mounted into epoxy for ease of handling and testing. After curing, the specimen was polished to a 600-grit surface finish. The specimen was then clamped into a flat cell arrangement, and connected to a Potentiostat (Model 273A). For each

polarization scan, the specimens were left to stabilize at open circuit for 2 hours. Three scans were attempted in each solution to insure consistency of data. All scans were run at a rate of 1.67×10^{-2} mV/s.

Anodic polarizations were run in sulfuric acid solutions. Acid concentration was varied (0.01M, 0.05M and 0.1M H_2SO_4) so was the molybdate concentration ($10^{-2} - 10^{-5}$ M Na_2MoO_4) to investigate the effect on anodic polarization behavior. Initially, tests were run in the lowest concentration acid solution, 0.01M H_2SO_4 , and varying inhibitor concentration from lowest to highest to view the effect on the anodic scan profile. Addition of molybdate was chosen in low concentrations to limit the effect on raising solution pH. Any large shift in pH would include an additional complication to the evaluation of the inhibitor and its effective concentration. It would be difficult to single out the cause of the reduction in electrolyte corrosivity.

For cathodic polarizations, inhibited borate buffer solutions were initially used to measure the effectiveness of Na_2MoO_4 and Na_2CrO_4 against uninhibited borate buffer control. $\text{Ce}(\text{acetate})_3$ and $\text{Zn}(\text{acetate})_2$ were used, with equivalent acetate concentrations, based on their reduction of HER rate and/or hydrogen absorption. $\text{Na}(\text{acetate})$ was used as a control solution to view the inhibiting effect of Ce^{3+} and Zn^{2+} . REM inhibitors were also utilized to investigate their effect on the HER.

Electrochemical Hydrogen Charging and Extraction (Potentiostatic) – Barnacle Electrode Method

To further screen inhibitor types, results from the previous cathodic polarization scans were used to determine critical inhibitor concentrations. Potentiostatic testing, "barnacle electrode method," was used to determine $C_{\text{H,diff}}$ at different inhibitor concentrations and η in UNS K92580. The barnacle electrode method consisted of using a thin sample of the material (1cm^2 exposed surface x 0.10mm thick) in the flat cell arrangement [12]. The sample was then connected to a Potentiostat and a cathodic potentiostatic hold was applied, below E_{H/H^+} , for a period of 48 hours to fully charge the sample with absorbed hydrogen. The overpotentials were varied to view the effect of inhibition in different conditions. After charging the samples with hydrogen, the samples were then removed from the inhibited electrolyte, cleaned with methanol and then inserted in a cell filled with borate buffer solution (pH 8.4). Another potentiostatic hold was applied just above E_{H/H^+} , $\eta = 330$ mV, to oxidize and extract hydrogen from the

samples. The measured hydrogen oxidation current density was used to calculate $C_{H,diff}$ by fitting the profile to the following expression [5,12]:

$$C_{H,diff} = \frac{J_H}{zF} \left(\frac{D_H}{\pi t} \right)^{-1/2} \quad - \text{Eq. 5}$$

where J_H is the hydrogen oxidation current density, z is the hydrogen atomic number (+1), t is the hydrogen extraction time, and F is Faraday's constant. A complexity is that D_H values depend on $C_{H,diff}$ diffused in the UHSS. This was previously analyzed and a correlating was used to determine $C_{H,diff}$ with greater accuracy [5]:

$$\log D_H = -0.416\eta - 08.14 (\text{at room temp.}) \quad - \text{Eq. 6}$$

Fracture Testing in Simulated Seawater Environments

A single edge notch specimen of UNS K92580 was machined, 10.2mm wide x 2.54mm thick. The notch was electrospark-machined to 0.065mm wide x 0.11mm deep. The specimen was fatigue precracked to 0.030mm deep in air. Finally, the specimen was fitted into a plexiglass cell and mounted into a fracture machine [1].

For anodic inhibition testing, the cell was initially filled with 0.6M NaCl (pH = 6.9) and tested then another run was run in 0.6M NaCl + 0.01M Na_2MoO_4 (pH = 7.1). Both solutions were aerated and had air bubbling into the cell to eliminate any solute precipitation in the stagnant solution. A Potentiostat was connected to the specimen to apply a constant η (slightly anodic) at a constant actuator displacement rate. For cathodic inhibition testing, the cell was first filled with 0.6M NaCl (pH = 6.9) then with 0.6M NaCl + 0.05M $\text{Ce}(\text{acetate})_3$ (pH = 6.9). As before, both solutions were aerated and had air bubbling into the cell. The Potentiostat was used to apply a constant cathodic η at a constant actuator displacement rate.

During all the experiments' run, the load (P), actuator displacement (δ), time (t), and direct current potential drop (dcPD) values were recorded. The crack length (a) was calculated using the dcPD method [4].

RESULTS

Anodic Polarization (Potentiodynamic) in Selected Anodic Inhibitors

As expected, the addition of inhibitor, even in low concentrations, enhanced corrosion resistance and passivity as seen in Fig. 5. Tests were continued with higher H_2SO_4 concentrations and similar results were achieved. The critical current density (J_{crit}) was measured in H_2SO_4 solutions first with no Na_2MoO_4 then with the gradual addition of the inhibitor. Figure 6 shows that the values trend with the concentration of both H_2SO_4 and Na_2MoO_4 in the solutions. The lowest acidity solution had the lowest values for the same molybdate concentration. Also, the specimens tend to passivate quicker with the addition of more inhibitor, as indicated by the decrease in the passivation potential (E_{pp}) in each H_2SO_4 solution concentration with increasing inhibitor concentration. Finally, the values for the corrosion current density (J_{corr}) were estimated based on a Tafel fit. The estimated values of J_{corr} decrease with the decrease of H_2SO_4 concentration and the increase in Na_2MoO_4 concentration. Further mass loss tests are planned to accurately quantify corrosion rates.

Figure 7 shows anodic scans that were attempted in aerated 0.6M NaCl solutions to simulate sea water environments. A major reduction in J_{corr} was noticed when adding 0.01M and 0.05M Na_2MoO_4 into the solution compared to uninhibited test solution. The pitting potential (E_{pit}) tends to increase with the addition of the molybdate inhibitor leading to the increase in the passive region as seen in Fig. 8.

Another set of tests are currently being conducted to view the benefit of the addition of $\text{Ce}(\text{acetate})_3$ to solutions containing Na_2MoO_4 .

Cathodic Polarization (Potentiodynamic) in Selected Cathodic Inhibitors

Initially, test scans were run in borate buffer as the control solution. Then in 0.1M of the inhibitor (Na_2MoO_4 or Na_2CrO_4) was added to view effect on lowering HER rate. Figure 9 shows that, with the addition of chemicals, a decrease in the specimen OCP and the HER rate, down to η between -0.2 and -0.3V. Overpotentials below this limit show an increase in the reaction rate, which was evident from the enhancement in H_2 bubbling off of the sample surface with more cathodic potentials. This was further shown in proceeding charging experiments as seen in Figures 13 and 14, further discussion is provided in the following

section. The addition of both chemicals resulted in an insignificant increase in pH. This was resolved by plotting the cathodic current densities (J_c) vs. η instead of E_{app} (Fig. 9).

Another set of experiments were performed in acetate-based solutions to test the effectiveness of Ce and Zn to inhibit HER rate. Initial analysis of the results show that $Ce(acetate)_3$ slightly raises HER rate compared to $Na(acetate)$, with similar acetate concentration. However, Figures 16 and 17 show that at higher η data indicate current decay in the 0.05M $Ce(acetate)_3$ solution producing less cathodic current densities (J_c) and HER charge (q_c) compared to 0.15M $Na(acetate)$. During polarization, a hydroxide film forms in the presence of $Ce(acetate)_3$ on the exposed specimen surface due to the increase in local pH to levels where Ce^{3+} is no more soluble in solution.

$Zn(acetate)_2$ was also used, with similar acetate concentration, to view affect on HER rate. Although, Zn^{2+} is known to drastically reduce HER in acidic solutions [18], it had minimal effect on it in the solutions with neutral acidity. Figure 15 shows that $Zn(acetate)_2$ shifts the HER current density less cathodic compared to the control. Also, $Zn(acetate)_2$ has a drastic effect on HER charge (q_c) as it indicate very low values in Fig. 17. Unfortunately, its use is limited to overpotentials above $\eta = -0.5V$, below which Zn deposits from solution. Again, the overpotentials were used instead of the applied potential to compensate for the difference in pH amongst the different solutions.

Hydrogen Charging and Extraction (Potentiostatic) – Barnacle Electrode Method

Hydrogen charging was performed by applying a potentiostatic hold below E_{H/H^+} to promote HER, as below discharge-recombination and/or absorption reactions:

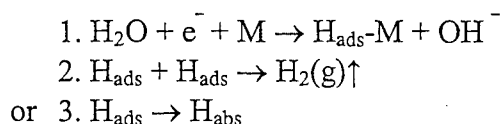


Figure 11 shows that as the overpotential (η) is decreased (more cathodic), the observed cathodic current density (J_c) decreases accordingly. The hydrogen oxidation current density (J_H) from extraction follows the overpotential values applied when charging the samples as seen for 0.15M $Na(acetate)$ in Fig. 12. The J_H profile correlates well with the square root of time.

Initially, hydrogen charging of UNS K92580 was performed in borate buffer (pH = 8.4) as a control solution. Scans were then attempted in borate buffer with added chemical inhibitors

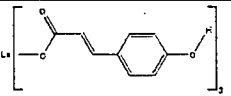
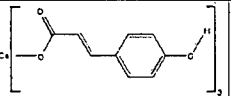
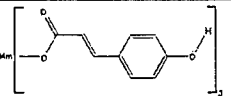
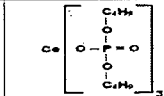
(Na_2MoO_4 and Na_2CrO_4) to test their effectiveness in reducing $C_{\text{H,diff}}$. Figure 13 shows that the hydrogen charging profiles decrease (more cathodic) with the addition of the chemicals. The HER charge density values for the inhibited solutions were significantly more cathodic than that of the uninhibited borate buffer solution as seen in Fig. 14. They correlate nicely with the applied η . Figure 18 indicates that the addition of both MoO_4^{2-} and CrO_4^{2-} did not decrease $C_{\text{H,diff}}$ compared to uninhibited borate buffer.

Again, acetate-based solutions were used to test the effectiveness of Ce and Zn compounds for inhibiting HER. Data at high overpotentials (less cathodic) suggest that $\text{Ce}(\text{acetate})_3$ exhibits more cathodic J_c (Fig. 15), while shifting the overpotential further cathodic shows much higher J_c (Fig. 16). While Figure 17 shows its effect on lowering q_c compared to $\text{Na}(\text{acetate})$ indicating its mitigation to HER. This reduction in q_c of the HER results in $\text{Ce}(\text{acetate})_3$ provided best inhibition and reduction of $C_{\text{H,diff}}$ for a wide range of applied η as seen in Fig. 18. During charging, a white film is noticed on the specimen surface indicating the deposition of $\text{Ce}(\text{OH})_3$ due to the shift in local pH at the sample/electrolyte interface. Ce^{3+} is not soluble in alkaline conditions, above pH = 9 [18].

On the other hand, $\text{Zn}(\text{acetate})_2$ showed limited reduction in $C_{\text{H,diff}}$ (Fig. 18), although analysis of the charging profiles indicates a major reduction in HER charge density (Figures 15 and 16). The profile from Fig. 16 shows a sloping profile with charging time. The associated charge density for this scan is 275 coulomb/cm^2 . This includes Zn deposition in addition to the HER. Once the amount of Zn is weighed and the charge associated with the deposition ($q_{\text{Zn}} = 257 \text{ coulomb/cm}^2$) is subtracted from the total current, the resulting q_c for $\text{Zn}(\text{acetate})_2$ at $\eta = -0.5\text{V}$ is still lowest, compared to both Ce and Na acetates as indicated in Fig. 17.

As a continuation to screening new inhibitors, rare earth metal (REM) organic inhibitors were chosen, refer to Table 6 [3]. In the cathodic conditions, a thin film is deposited on the surface of the hydrogen charged specimen, similar to the behavior in $\text{Ce}(\text{acetate})_3$. But without the analysis of the film this could not be verified.

Table 6 – Properties of the rare earth metal organic inhibitors [17]

No.	1	2	3	4
REM Organic Inhibitor	Lanthanum 4-hydroxy cinnamate	Cerium 4-hydroxy cinnamate	Lanthanoides* hydroxy cinnamate	Cerium dibutyl phosphate
Chemical Formula	$\text{La}(\text{C}_9\text{H}_8\text{O}_3)_3 \cdot 5\text{H}_2\text{O}$	$\text{Ce}(\text{C}_9\text{H}_8\text{O}_3)_3 \cdot 5\text{H}_2\text{O}$	$\text{Mm}(\text{C}_9\text{H}_8\text{O}_3)_3 \cdot 5\text{H}_2\text{O}$	$\text{Ce}(\text{C}_8\text{H}_{18}\text{O}_4\text{P})_3$
Molecular Formula				
MW (g/mol) - anhydrous	627.90	629.10	629.96	767.1
MW (g/mol) - hydrated	717.98	719.18	720.04	NA
Solubility Limit **	960 ppm (sugg. 400 - 800 ppm)	800 ppm (sugg. 300 - 600 ppm)	800 ppm (sugg. 300 - 700 ppm)	not determined

*Mm Elements	Sc	La	Ce	Pr	Nd	Gd	Tb	Dy	Er	Yb
Weight %	0.001	24.251	52.698	5.492	14.684	2.24	0.093	0.318	0.114	0.001

Cerium dibutyl phosphate, $\text{Ce}(\text{dbp})_3$, showed similar q_c and $C_{H,\text{diff}}$ when compared to the control solution $\text{Na}(\text{dbp})$, at similar dibutyl phosphate concentrations. On the other hand, $\text{La}(4\text{-OHcinnamate})_3$ and $\text{Mm}(4\text{-OHcinnamate})_3$ showed very good protection at very low concentrations, 50-200 ppm, with similar solution conductivity as $\text{Na}(\text{dbp})$. Tests in control solutions are being conducted to verify inhibition.

Finally, the diffusible hydrogen concentration ($C_{H,\text{diff}}$) values for all inhibitors, except REM inhibitors, are reported vs. the square root of cathodic current density (J_c) as seen in Figures 19 and 20, because of the theoretical connection, refer to the discussion section. Again, the figures show that $\text{Ce}(\text{acetate})_3$ is most effective in reducing $C_{H,\text{diff}}$ in a wide range of η (Fig. 18). $\text{Zn}(\text{acetate})_2$ does not reduce $C_{H,\text{diff}}$ compared to control, but it reduces tremendously the HER current density (Fig. 17). Further analysis is made in the discussion section.

Fracture Testing in Inhibited Sea-water Solutions

UNS K92580 was tested in 0.6M NaCl + 0.01M Na_2MoO_4 (pH ~ 7.1) with a pre-crack length of 0.76 mm. The load was increased to a K of 100 MPa $\sqrt{\text{m}}$. The crack growth was inhibited, compared to the uninhibited case. The potential was held at a cathodic potential (-0.5V_{SCE}) to the bulk surface in the inhibited solution but not in uninhibited 0.6M NaCl. There was very little crack growth as seen in Figure 21. The potential was then increased above OCP to -0.4 V_{SCE}. Initially, no crack growth was observed since the net current was still cathodic. After 20 hours, dissolution of the metal commenced with an increase in anodic current resulting in significant acidification (Fig. 22) leading to substantial growth of the crack, 2.5mm in ~ 7 hours as seen in Fig. 21. The threshold stress intensity was restored to highest value at -0.5V_{SCE} but not at -0.4V_{SCE} as seen in Fig. 25.

Further analysis of a rescaled crack with a gap of 1.5 mm showed that Na_2MoO_4 inhibited the anodic reaction rate and prevented crack tip acidification at anodic potentials as seen in Fig 22. This effect was minimal in a rescaled crack with a gap of 5mm over the time period examined due to the effect of the oxygen reduction reaction in the rescaled crack. Results from applied cathodic potentials verified barnacle cell results showing that molybdate does not directly inhibit the cathodic reaction rate, but would limit cathodic current at open circuit through anodic inhibition. At highly cathodic or anodic potentials, the local E and pH at the crack tip can lead to H^+ reduction and subsequently H absorption [16].

In another test, 0.05M $\text{Ce}(\text{acetate})_3$ was used in 0.6M NaCl to investigate its effectiveness in blocking hydrogen uptake. A specimen was used with a fatigue pre-crack of 2.5 mm. Results indicate no protection of sample resulting in fracture data resembling that of uninhibited environment at similar conditions as seen in Fig. 23. This could be attributed to not alloying enough time for $\text{Ce}(\text{OH})_3$ to form onto the crack surface, although SEM micrographs show some patchy formation of the film on the pre-crack region of the specimen, but not full coverage (Fig. 24). This could be due to the dislodging of the film when cleaning the specimen with methanol/acetone before inserting it into the SEM chamber. The color of the film resembles that formed when charging specimen in the barnacle electrode method. Also, this film did not appear in the uninhibited NaCl solution concluding it being the hydroxide film.

DISCUSSION

Anodic Inhibition

Under crack anodic conditions, at high local potentials, metal dissolution occurs and hydrolysis follows releasing H^+ , as shown in the below reactions. The released H^+ could then be reduced on the material's bulk surfaces and either recombine and bubble off as H_2 gas or become absorbed into the material causing its embrittlement and cracking. To eliminate HEE and HEAC from occurring, anodic inhibitors are utilized to mitigate metal oxidation.

1. $\text{M} \rightarrow \text{M}^+ + \text{e}^-$ (metal oxidation)
2. $\text{M}^+ + \text{H}_2\text{O} \rightarrow \text{MOH} + \text{H}^+$ (hydrolysis)

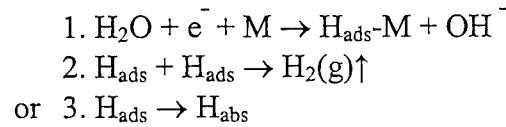
In general, the anodic polarization scans in H_2SO_4 develop more stable passive films as the amount of inhibitor is increased and the active dissolution rates are lowered. The critical current density (J_{crit}) showed a decrease when increasing inhibitor concentration leading to

quicker passivation. In 0.1M H₂SO₄, J_{crit} was reduced from 2.3x10⁻² to 2.7x10⁻³ A/cm². As previously mentioned, the inhibitor concentrations were limited to very low concentrations to limit the increase in solution pH value.

Fracture testing in 0.6M NaCl + 0.01M Na₂MoO₄ (pH ~ 7.1) showed that crack growth was inhibited at an applied potential of -0.5V_{SCE}. Also, no net cracking was initially observed after raising the potential above OCP to -0.4 V_{SCE}. This was due to the inhibition of the anodic reaction rate and the prevention of crack tip acidification at anodic potentials. After 20 hours, dissolution of the metal commenced with an increase in anodic current and the crack grew 2.5mm in 7 hours.

Cathodic Inhibition

In crack cathodic conditions, the production of H⁺ and its absorption into metal occurs by the coupled discharge-recombination hydrogen evolution reaction (HER), as follow, where reactions 1 and 2 occur at the same rates [13]:



As such, the cathodic current density is defined as:

$$J_c = J_0 \exp\left(\frac{-\alpha\eta F}{2RT}\right) = k_r \theta^2 \quad - \text{Eq. 8}$$

where J₀ is the exchange current density on for HER on Fe surface, α is the transfer coefficient, k_r is the recombination rate constant for adsorbed hydrogen on the surface, and θ is the surface coverage of adsorbed hydrogen on the surface.

The steady state lattice hydrogen concentration (C_H) is also a function of hydrogen surface coverage and is defined as following at equilibrium:

$$C_H = \frac{k_{\text{abs}}}{k_{\text{des}}} \theta \quad - \text{Eq. 9}$$

where k_{abs} is the absorption rate constant for hydrogen and k_{des} is the desorption rate constant for hydrogen at the surface.

Finally, an expression can be written to relate the lattice hydrogen concentration and the water reduction reaction rate at the surface by combining equations 8 and 9:

$$C_H = \left(\frac{k_{abs}}{k_{des}} \right) \left(\frac{J_c}{k_r} \right)^{1/2} = \left(\frac{k_{abs}}{k_{des}} \right) \left(\frac{J_0}{k_r} \right)^{1/2} \exp \left(\frac{-\alpha \eta F}{2RT} \right) \quad - \text{Eq. 10}$$

The data associated with Na_2MoO_4 and Na_2CrO_4 showed that both had little or no effect on $C_{H,diff}$ when compared to the control solution and at similar η . Although the hydrogen production charge associated with both inhibitors showed an increase, this may have been offset by an increase in recombination or desorption rates or a decrease in absorption rate since C_H remained unchanged (Eq. 10). These anodic inhibitors have no cathodic inhibition abilities.

On the other hand, $\text{Ce}(\text{acetate})_3$ showed best inhibition of $C_{H,diff}$ in a wide range of η . $\text{Ce}(\text{acetate})_3$ showed lower q_c (hence J_c) compared to $\text{Na}(\text{acetate})$ for the same applied η , especially at potentials more negative than -0.4V. In a fracture experiment, 0.05M $\text{Ce}(\text{acetate})_3$ was used in 0.6M NaCl to investigate its effectiveness in blocking hydrogen uptake. Results indicate no protection of sample resulting in fracture data resembling that of uninhibited environment at similar conditions. This could be attributed to not allowing enough time for $\text{Ce}(\text{OH})_3$ to form onto the crack surface, although SEM micrographs show some patchy formation of the film on the pre-crack region of the specimen, but not full coverage.

The use of $\text{Zn}(\text{acetate})_2$ further lowered q_c , when compared to $\text{Na}(\text{acetate})$ and $\text{Ce}(\text{acetate})_3$, but with no significant effect on $C_{H,diff}$. Further analysis shows that indeed $\text{Zn}(\text{acetate})_2$ lowers J_c to values lower than that of the control solution. But the sharp decrease in J_c might have been offset by an increase in hydrogen absorption rate into the materials and/or a decrease in hydrogen desorption and recombination rates. Either of these factors could explain the limited effect of the lower values for J_c on the diffusible hydrogen concentration.

Analysis of the REM organic inhibitors show that they exhibit lowest current densities (J_c) compared to all other inhibitors. This might be promising, but could be attributed to the high resistivity of the solution altering the true potential applied, so tests in a control solution is

being conducted. But this could also be due to a decrease in HER rate. The values for $C_{H,diff}$ using these inhibitors are equal or better than in $Ce(acetate)_3$, at similar J_c .

CONCLUSIONS

- An active-passive transition developed when anodically polarizing UNS K92580 in inhibited acid solutions. The inhibition also led to a reduction in the corrosion current density in the active range.
- Fracture testing in 0.6M NaCl + 0.01M Na_2MoO_4 showed that environmental crack growth was inhibited when initially raising the potential above OCP to $-0.4V_{SCE}$. Na_2MoO_4 inhibited the anodic reaction rate and prevented crack tip acidification. Cracking only occurred after 20 hours, after general dissolution of the metal commenced with an increase in anodic current.
- There was no apparent advantage from the use of Na_2MoO_4 or Na_2CrO_4 as cathodic inhibitors, since they did not lower $C_{H,diff}$ at any cathodic potential.
- $Ce(acetate)_3$ showed best cathodic inhibition of $C_{H,diff}$ in a wide range of η . It lowered J_c , especially at potentials more negative than $-0.4V$.
- The addition of 0.05M $Ce(acetate)_3$ to 0.6M NaCl did not protect against hydrogen uptake and cracking in a fracture experiment. This could be attributed to not alloying enough time for $Ce(OH)_3$ to form onto the crack surface.
- The use of $Zn(acetate)_2$ resulted in lowest q_c values, but with no significant decrease in $C_{H,diff}$. This might have been offset by an increase in k_{abs} and/or a decrease in k_{des} and k_r .
- The use of the REM organic inhibitors result in lowest J_c and $C_{H,diff}$ values compared to all other inhibitors. Additional testing is being conducted to verify the results. This might be promising, but could be attributed to the high resistivity of the solution. This could also be due to a decrease in HER rate at a given η .

ACKNOWLEDGEMENTS

The authors acknowledge Dr. Airan Perez, Program Officer from the Office of Naval Research for the support, ONR Contract No. N00014-03-1-0029. Beth A. Kehler and Yongwon Lee are acknowledged for their support on the research project. All experiments were conducted at the Center for Electrochemical Science and Engineering. All electrochemical

instruments and software were provided by Princeton Applied Research and Scribner Associates, Inc. Finally, Sami M. Al-Ghamdi acknowledges the support and academic sponsorship provided by Saudi Aramco Oil Company.

REFERENCES

- [1] J.R. Scully, B.A. Kehler, Y. Lee, and R.P. Gangloff, Tri-Service Corrosion, No. 06T019, Orlando, FL, (2005)
- [2] D. Li, R.P. Gangloff, J.R. Scully, Met. and Materials Trans. A, 35A, pp. 849-864 (2004)
- [3] F. Blin, S.G. Leary, K. Wilson, G.B. Deacon, P.C. Junk, M. Forsyth, J. Appl. Electrochem., 34, pp. 591-599 (2003)
- [4] R.L.S. Thomas, J.R. Scully, R.P. Gangloff, Met. and Materials Trans. A, 34A, pp. 327-344, (2003)
- [5] R.L.S. Thomas, D. Li, J.R. Scully, R.P. Gangloff, Met. and Materials Trans. A, 33A, pp. 1991-2004 (2002)
- [6] C.J. McMahon, Jr., Eng. Fract. Mech., 68, pp. 773-788 (2001)
- [7] D.G. Enos, A.J. Williams, Jr., G.G. Clemena, and J.R. Scully, CORROSION/98, 54, No. 5, pp. 389-402, NACE Int'l., Houston, TX, (1998)
- [8] W.W. Gerberich, P.G. Marsh, J.W. Hoehn, *Hydrogen Effects in Metals*, TMS, Warrendale, PA, (1996).
- [9] P. Buckley, B. Placzankis, J. Beatty, R. Brown, Corrosion/94, No. 547, NACE Int'l, Houston, TX, (1994).
- [10] R. Ayer and P.M. Machmeier, Met. and Materials Trans. A, 24A, pp. 1943-1955, (1993).
- [11] V.S. Agarwala, *Modification of Crack Tip Chemistry to Inhibit Corrosion and SCC of High Str. Alloys In Embrittlement by the Local Crack Tip Environment*, Met. Soc. Of AIME, R.P. Gangloff, (1983).
- [12] J.J. Deluccia, D.A. Berman, Electrochemical Corrosion Testing, ASTM STP 727, pp. 256-273, (1981)
- [13] P.K. Subramanyan., *Comprehensive Treatise of Electrochemistry*, Plenum Press, New York, (1981).
- [14] C.T. Lynch, K.J. Bhanasali, P.A. Parrish, *Inhibition of Crack Propagation of High Strength Steels through Single and Multi-functional Inhibitors*, ARML-TR-76-120, Wright Patterson (1976).
- [15] R. A. Oriani, Hydrogen in metals, Conf. Proc.: Fund. Aspects of Stress Corr. Cracking in 1967, 32-50. NACE Int'l, Houston, TX (1969)
- [16] B.A. Kehler, S.M. Al-Ghamdi, Tri-Service Corrosion Conf. Poster, Orlando, FL, (2005)
- [17] S.M. Al-Ghamdi, CORROSION/06, Student Poster, San Diego, CA, (2006)
- [18] M. Pourbaix, *Atlas of Electrochemical Equilibria in Aqueous Solutions*, NACE Int'l, Houston, TX, (1974).

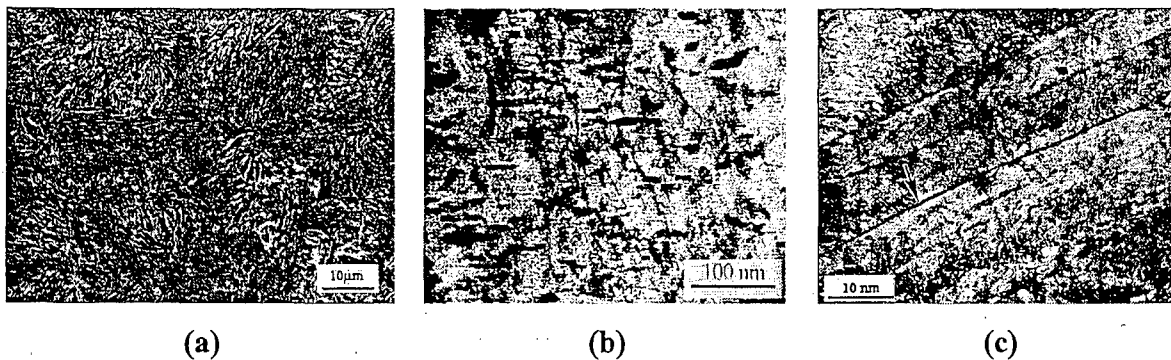


Fig. 1 – Microstructural features in UNS K92580: (a) the martensite packets, (b) fine dispersed M₂C carbides, and (c) reverted austenite on the martensite lath boundaries [10]

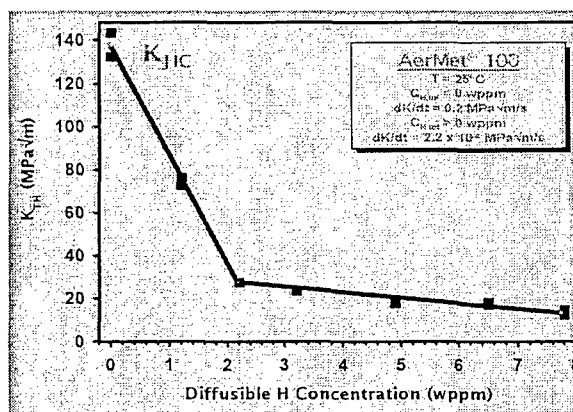


Fig. 2 – Dependence of K_{TH} on $C_{H,diff}$ in UNS K92580 [4]

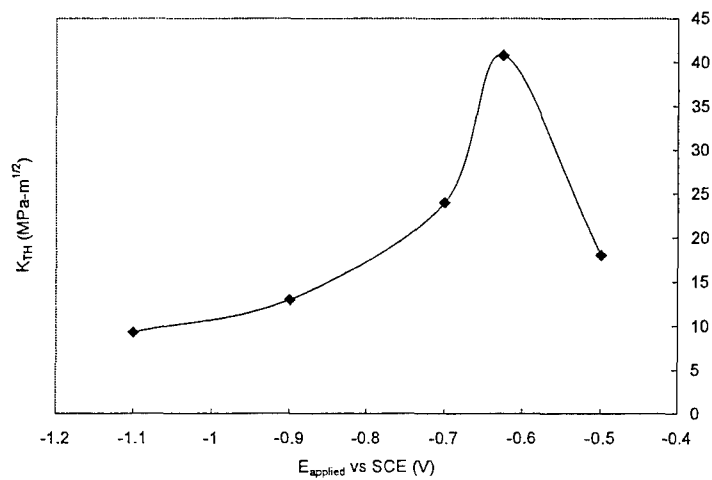


Fig. 3 – K_{TH} values vs. E_{app} for UNS K92580 in 0.6M NaCl. [1]

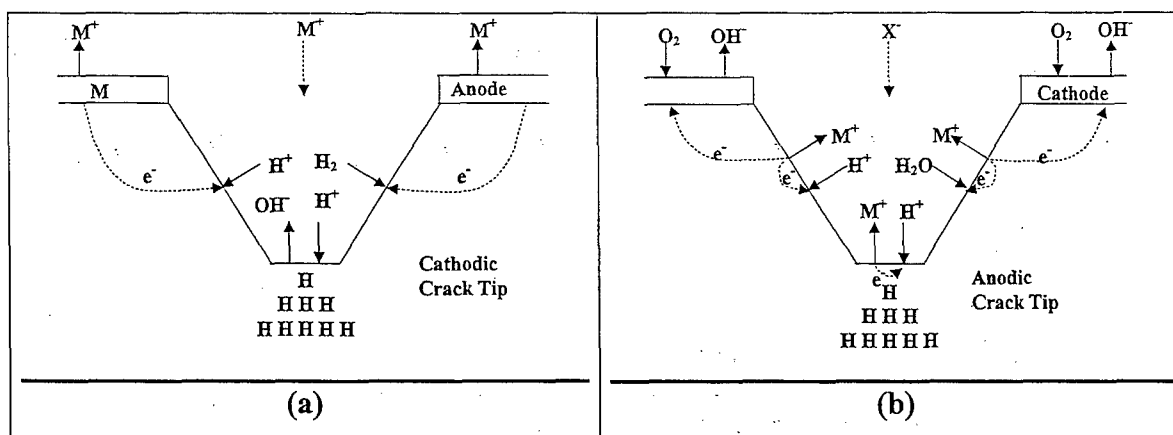


Fig. 4 – Schematic view of crack tip under: (a) cathodic conditions and (b) anodic conditions [16]

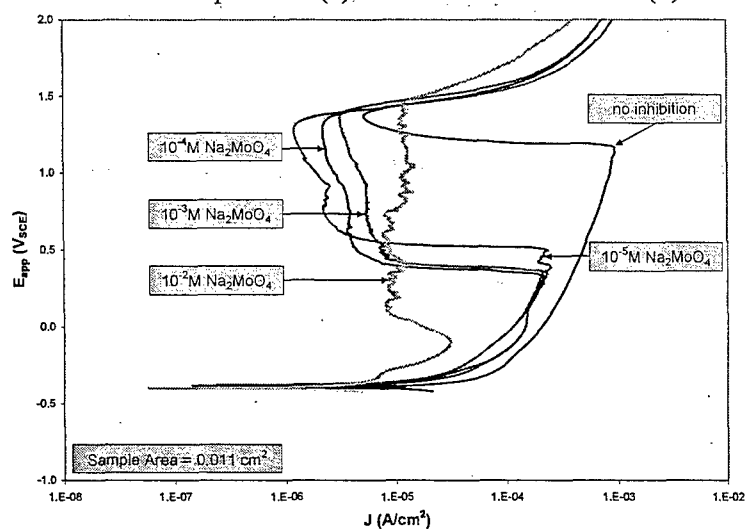


Fig. 5 – Anodic polarization profiles in 0.01M H_2SO_4 (deaerated, pH = 1.7, T = 23°C) [17]

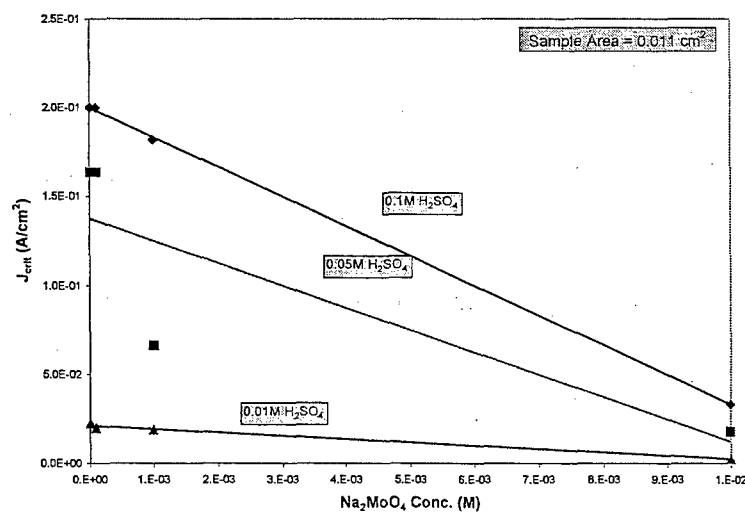


Fig. 6 – Evolution of the critical current density with Na_2MoO_4 conc. in H_2SO_4 solutions (deaerated, T = 23°C) [17]

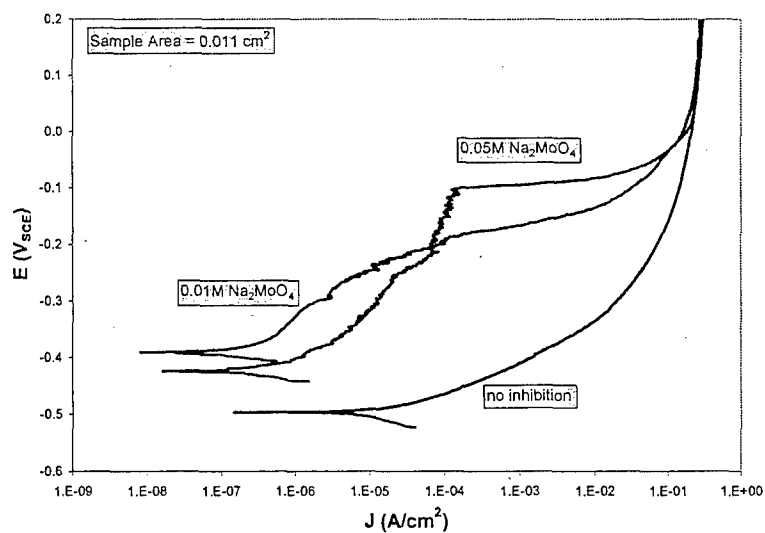


Fig. 7 – Anodic polarization profiles in 0.6M NaCl solutions (deaerated, pH = 7.1, T = 23°C) [17]

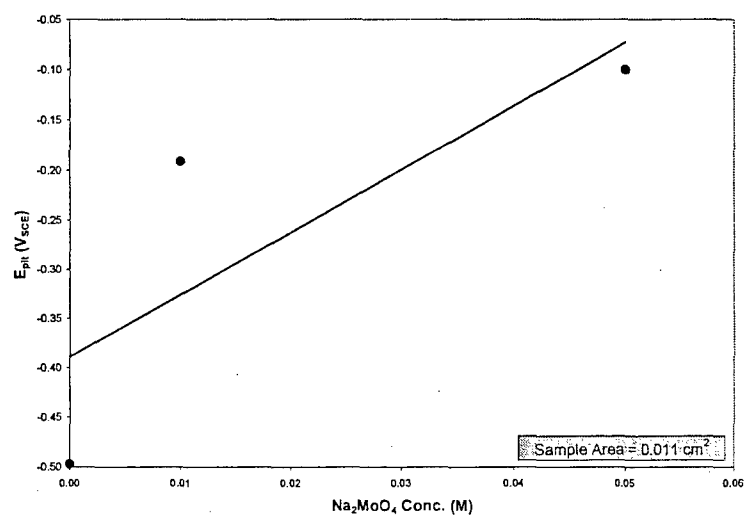


Fig. 8 – Evolution of the pitting potential with Na_2MoO_4 concentration in 0.6M NaCl solutions (deaerated, pH = 7.1, T = 23°C)

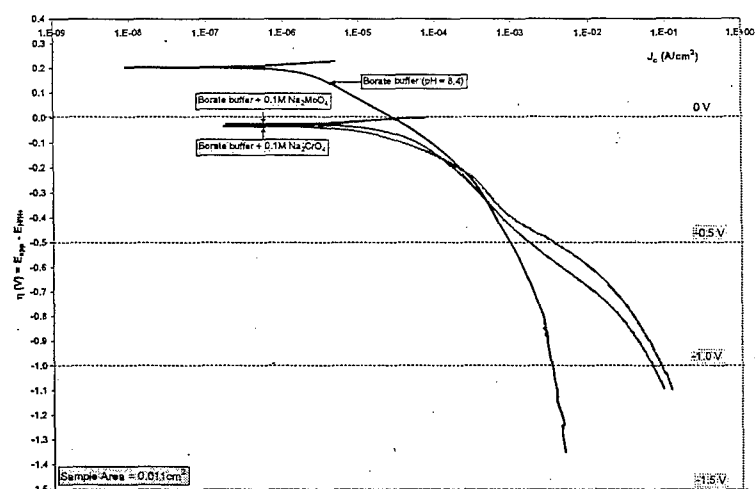


Fig. 9 – Cathodic polarization profiles in borate buffer solutions (deaerated, pH = 8.4, T = 23°C)

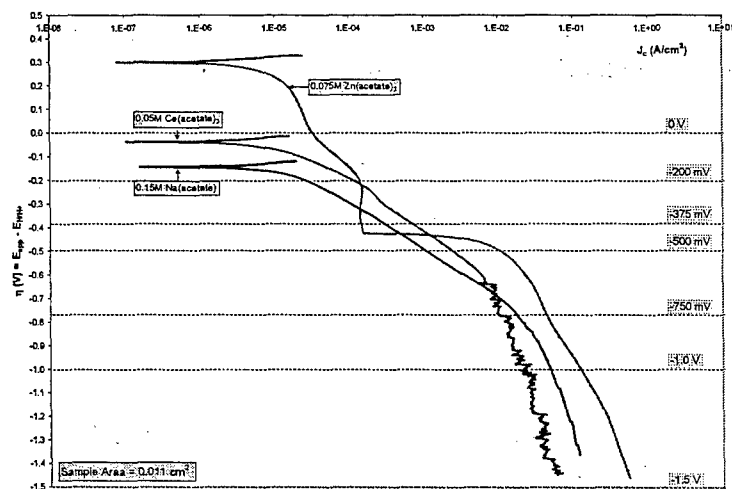


Fig. 10 – Cathodic polarization profiles in acetate-based solutions (deaerated, T = 23°C)

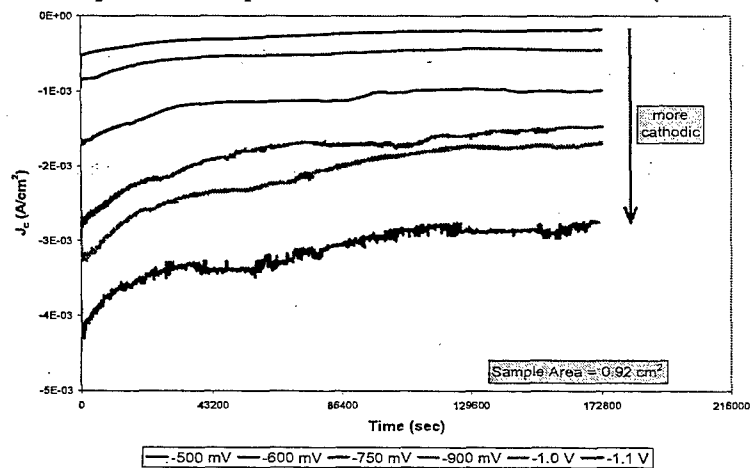


Fig. 11 – Effect of η on the hydrogen charging profiles in 0.05M Na(acetate) (deaerated, pH = 7.9, T = 23°C) [17]

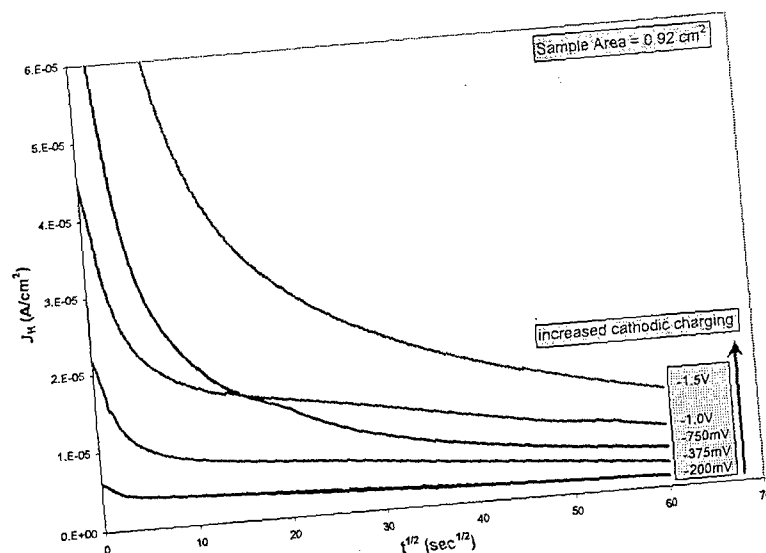


Fig. 12 – Hydrogen extraction profiles in borate buffer correlation with previous hydrogen charging η in 0.15M Na(acetate), (deaerated, pH = 8.4, T = 23°C).

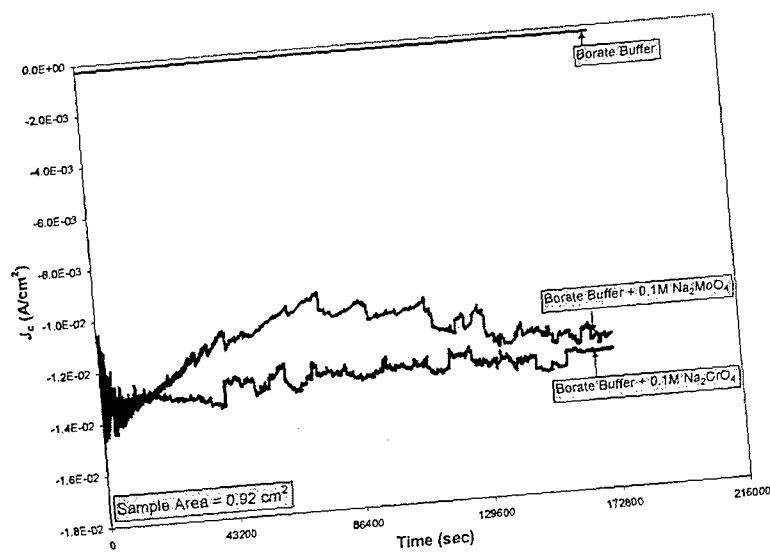


Fig. 13 – Hydrogen charging profiles in borate buffer solutions (deaerated, $\eta = -1.0V$, pH = 8.4, T = 23°C).

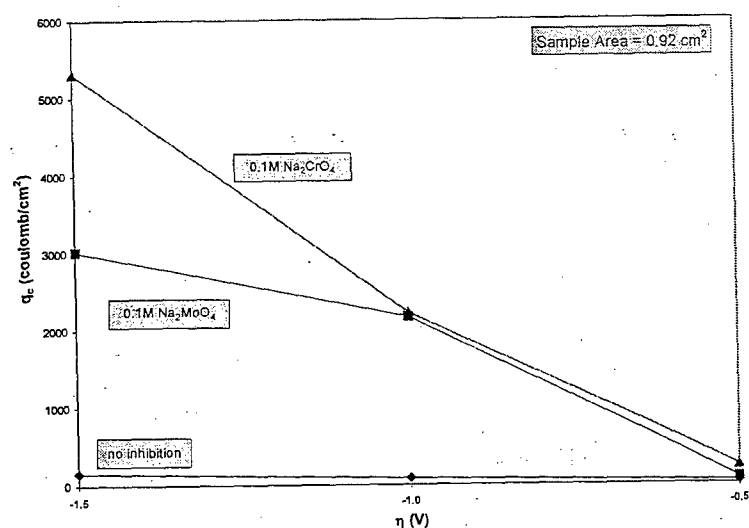


Fig. 14 – Hydrogen evolutions reaction charge density measured against applied η in borate buffer solutions (deaerated, pH = 8.4, T = 23°C)

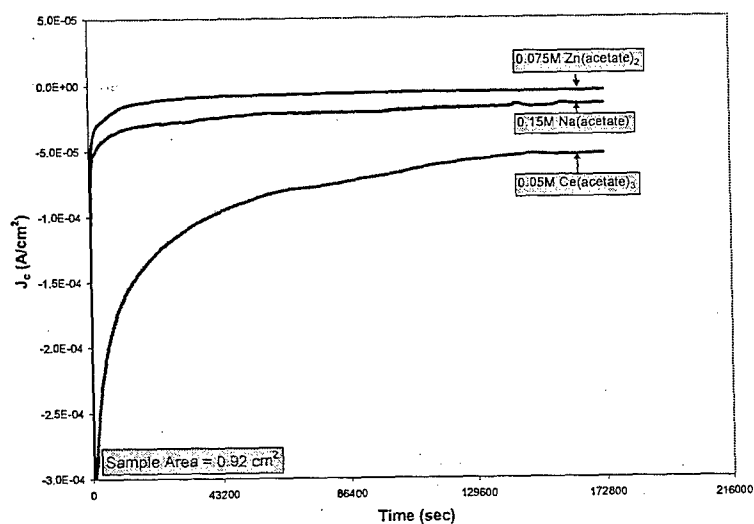


Fig. 15 – Hydrogen charging profiles in acetate-based solutions (deaerated, $\eta = -0.375V$ pH = 8.2 for Na(ac), pH = 6.9 for Ce(ac)₃, pH = 6.8 for Zn(ac)₂, T = 23°C)

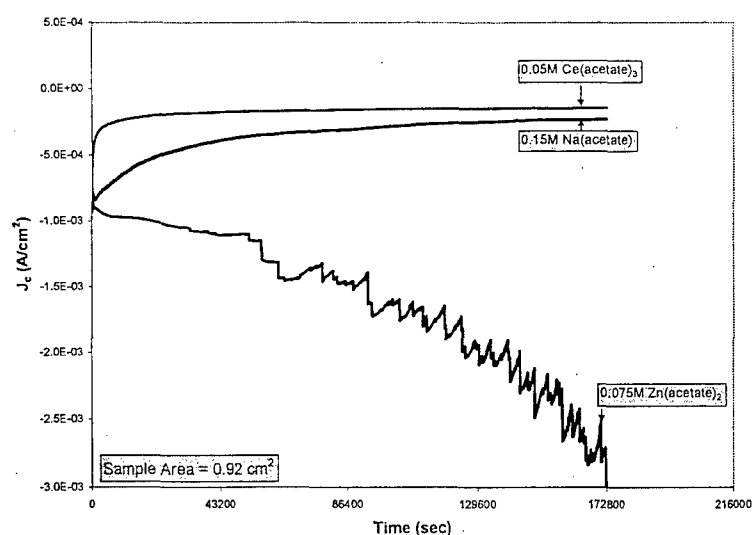


Fig. 16 – Hydrogen charging profiles in acetate-based solutions (deaerated, $\eta = -0.5\text{V}$ pH = 8.2 for Na(ac), pH = 6.9 for Ce(ac)₃, pH = 6.8 for Zn(ac)₂, T = 23°C)

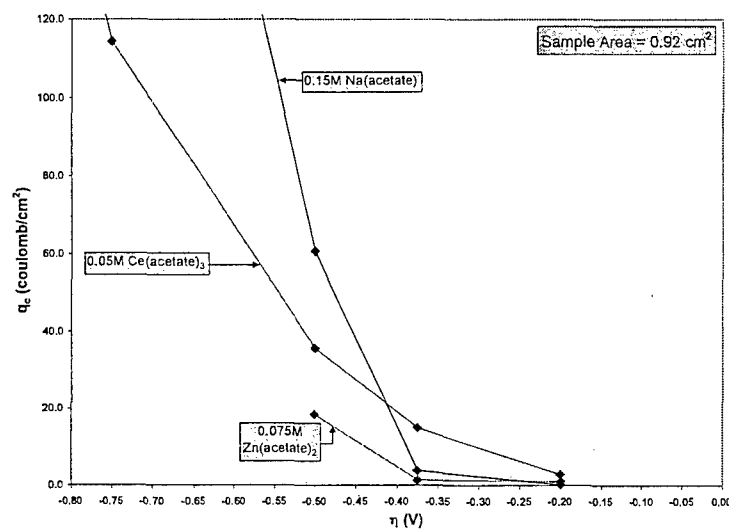


Fig. 17 – Hydrogen evolution reaction charge measured against applied η in acetate-based solutions (deaerated, pH = 8.2 for Na(ac), pH = 6.9 for Ce(ac)₃, pH = 6.8 for Zn(ac)₂, T = 23°C) [17]

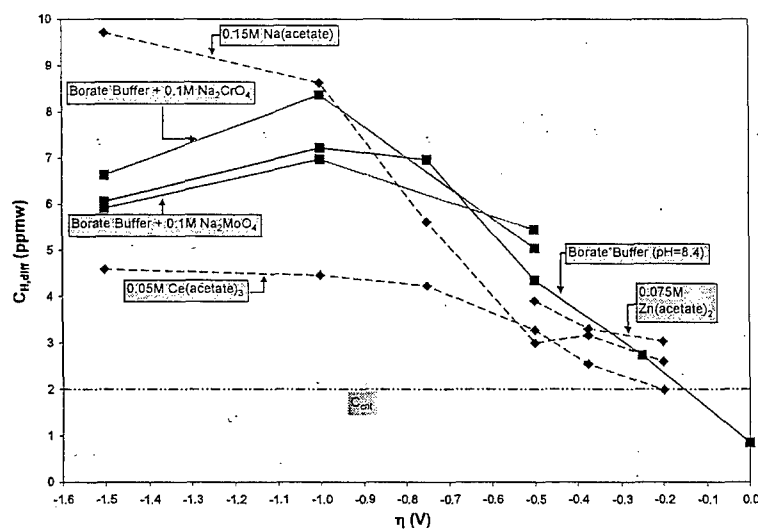


Fig. 18 – Diffusible hydrogen concentration vs. applied η for diff. inhibitor solutions (deaerated, pH = 8.4 for borates, pH = 8.2 for Na(ac), pH = 6.9 for Ce(ac)₃, pH = 6.8 for Zn(ac)₂, T = 23°C) [17]

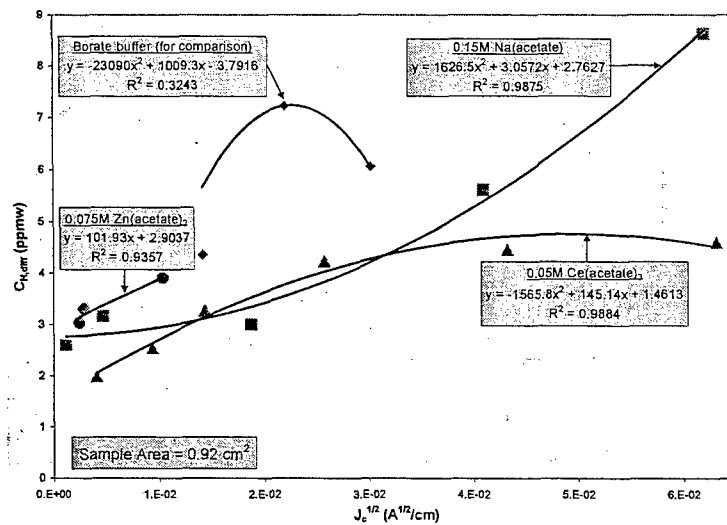


Fig. 19 – Diff. H conc. measured against the square root of cathodic current in acetate solutions (deaerated, pH= 8.4 for borate, pH= 8.2 for Na(ac), pH= 6.9 for Ce(ac)₃, pH= 6.8 for Zn(ac)₂, T= 23°C)

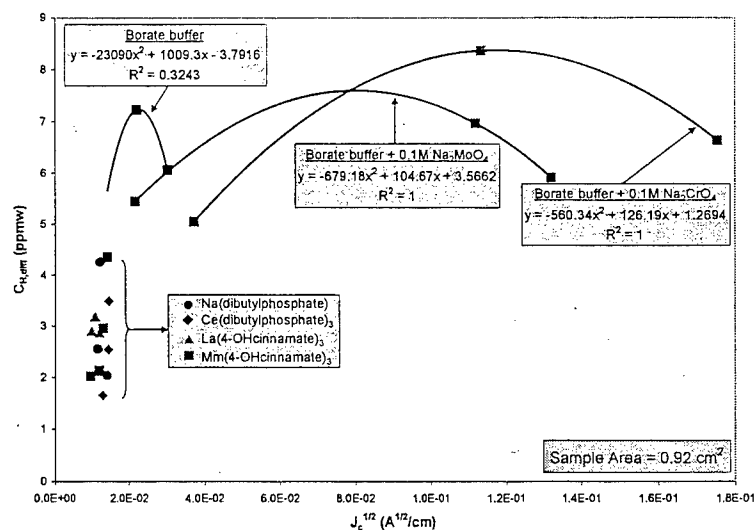


Fig. 20 – Diff. H conc. measured against the square root of cathodic current density in inhibitor solutions (deaerated, pH = 8.4 for borates, pH = 5.4 for dbp, pH = 6.0 for cinnamates, T = 23°C)

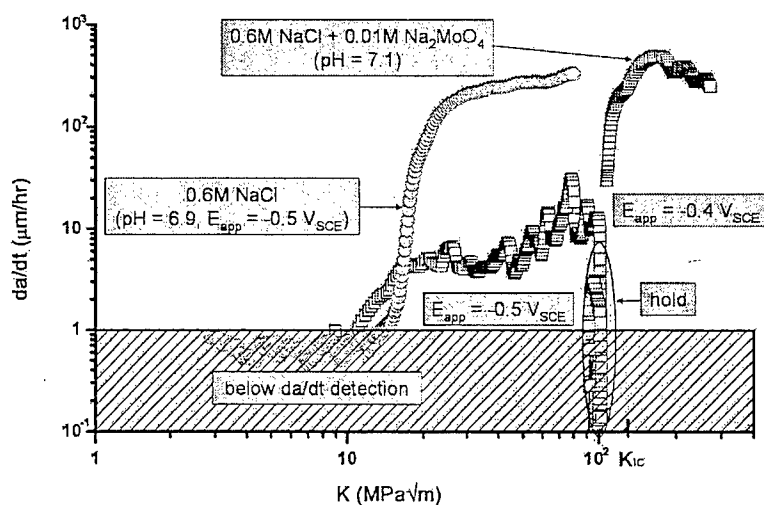


Fig. 21 – Effect of Na_2MoO_4 on da/dt in 0.6M NaCl (aerated, pH = 7.1, $E_{app} = -0.5V_{SCE}$, T = 23°C) [16,17]

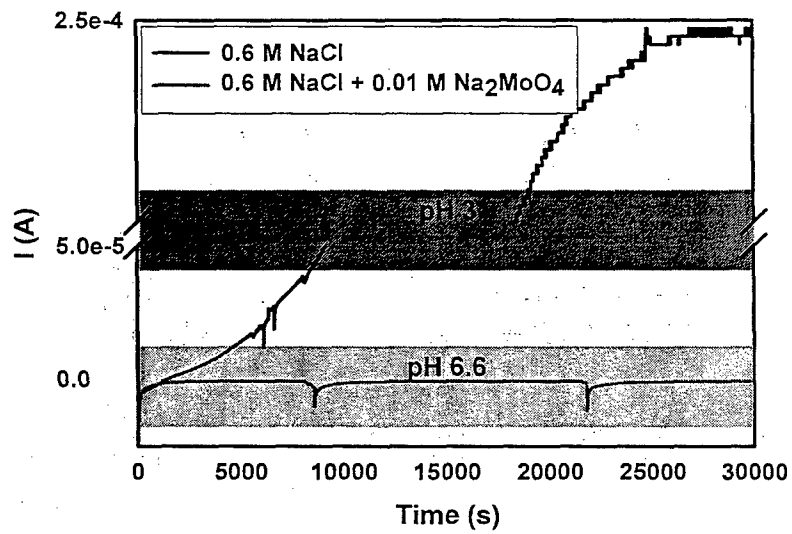


Fig. 22 – Current profile with time a rescaled crack in 0.6 M NaCl + 0.01 M Na₂MoO₄ (aerated, crevice gap = 1.5 mm, $E_{app} = -0.4V_{SCE}$) [16]

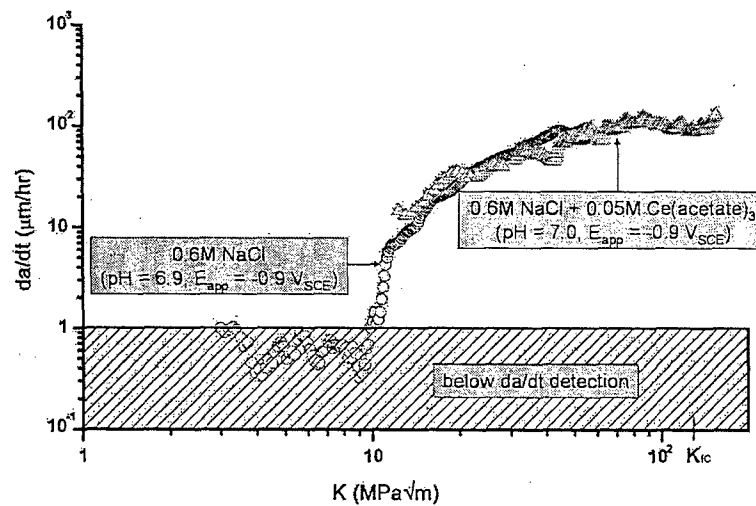


Fig. 23 – Effect of Ce(acetate)₃ on da/dt in 0.6M NaCl (aerated, pH= 7.0, $E_{app} = -0.9 V_{SCE}$, T = 23°C) [16,17]

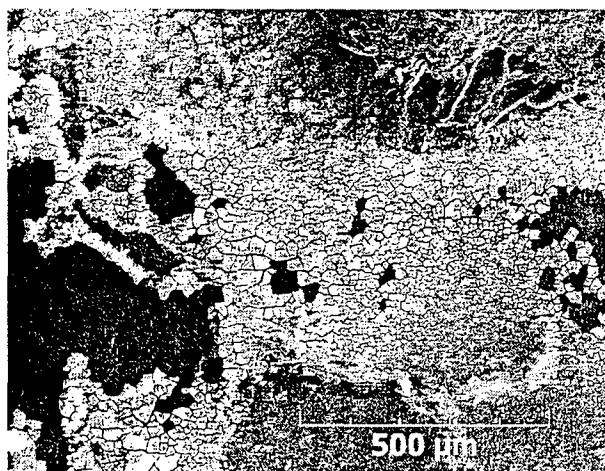


Fig. 24 - SEM micrograph of UNS K92580 pre-crack surface partially covered with Ce(OH)_3 [Y. Lee, 2005]

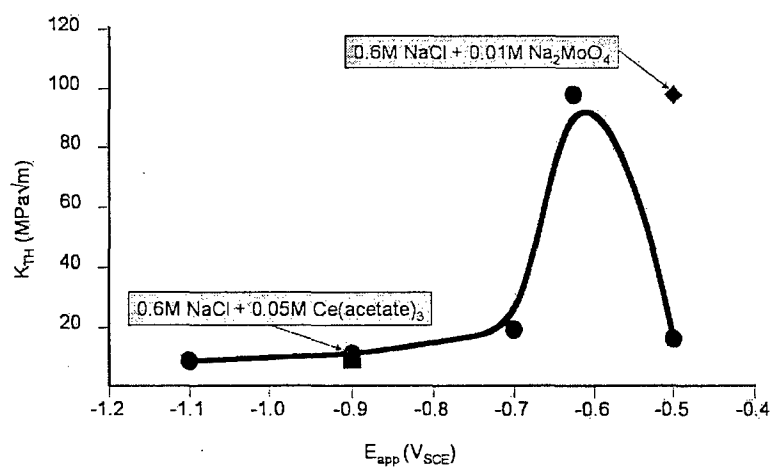


Fig. 25 – K_{TH} profile vs. E_{app} for UNS K92580 in 0.6M NaCl (Aerated, pH ~ 6.9 - 7.1, $T = 23^\circ\text{C}$) [16,17]